Flat bands and electronic localization in twisted bilayer graphene nanoribbons

Elias Andrade [1,*], Pierre A. Pantaleón [2], Francisco Guinea [2,3,4] and Gerardo G. Naumis [5,†]

[1]*Posgrado en Ciencias Físicas, Instituto de Física, Universidad Nacional Autónoma de México (UNAM). Apdo. Postal 20-364, 01000 México D.F., México*
[2]*IMDEA Nanoscience, Faraday 9, 28049 Madrid, Spain*
[3]*Donostia International Physics Center, Paseo Manuel de Lardizábal 4, 20018 San Sebastián, Spain*
[4]*Ikerbasque, Basque Foundation for Science, 48009 Bilbao, Spain*
[5]*Departamento de Sistemas Complejos, Instituto de Física, Universidad Nacional Autónoma de México (UNAM). Apdo. Postal 20-364, 01000 México D.F., México*

We analyze the electronic structure of twisted bilayer graphene (TBG) nanoribbons close to the magic angle. We describe a transition from an incomplete to a complete moiré structure. By considering *zigzag* and *armchair* edge terminations, the low-energy bands are strongly modified, and thus, the edge flat-band localization is sensitive to the type of boundary. By means of a scaled tight-binding model, we calculate the band structure and find that, for an *armchair* configuration, an incomplete moiré edge suppresses the edge localization, while for a *zigzag* configuration, we find a strong interference of the edge states with the moiré bands. In particular, for the *armchair* termination, we observe a competition between the ribbon periodicity and the graphene monolayers, which we describe with a potential well toy model. Furthermore, for ribbons with widths of multiple moiré cells, the flat bands of the moirés in the bulk are unperturbed as we change the borders. These results are explained in terms of the strong electronic localization, nearly Gaussian, in the *AA* stacking regions, as confirmed by an inverse participation ratio analysis. Our results demonstrate that the electronic structure of TBG nanoribbons is sensitive to the edge termination, offering an explanation for recent experimental results.

I. INTRODUCTION

Due to the interplay between nontrivial band topology and band flatness, magic-angle twisted bilayer graphene (TBG) has shown to be an ideal platform for the appearance of a plethora of topological and correlated phases, including, for example, nonconventional superconductivity [1,2], correlated insulators [3–5], ferromagnetism [6], and other many-body effects [7–24]. For magic angles the flat bands near the Fermi energy appear due to the localization of the electronic wave function at the *AA* stacking sites; this was predicted [25–27] and then experimentally confirmed [16,28–31]. The wave-function geometry comes from the modulated interlayer coupling, which can be seen as an effective moiré potential well [32–37].

Studies of TBG with reduced translational symmetry, for example, in flakes, have shown that a single moiré cell may be enough to localize the wave function in the *AA* spots [38], supporting a "moiré quantum well" picture. However, theoretical [39–42] and experimental [43,44] studies have demonstrated that in TBG with nanoribbon geometry, there are states localized at the *AA* regions in both the bulk and those near the edges. We refer as "moiré edge states" to the states localized at the *AA* regions closest to the borders; these may have a complete or incomplete moiré cell. On the other

hand, the term edge states will be used as usual to refer to the states localized at the *zigzag* borders of the honeycomb lattice. In particular, it has been shown that in the presence of a *zigzag* termination there is a coexistence of moiré states and edge states near the Fermi energy [44], and that the edge states are found at the edges of *AB* sites [39,40].

On the other hand, recent experiments have shown the breakdown of moiré flat bands in TBG due to edge termination [45]. In the experiment, the electronic localization is found to be persistent even if translational symmetry is broken as long as the moiré supercell is complete. However, when the supercell is incomplete, there is a strong suppression of the electronic localization, resulting in a vanishing of the density of states near the Fermi energy.

A useful methodology to analyze the transition from a complete to an incomplete supercell is by introducing an interlayer sliding between graphene layers, where the displacement between layers is particularly relevant in terminated TBG due the change in the borders at both the scales of the moiré lattice and the graphene lattice. This type of displacement is known to produce a topological charge pumping in the perpendicular direction of the displacement, characterized by a topological invariant known as the sliding Chern number [46–49].

In spite of this, while the topological sliding properties provide a description of the number of moiré edge states, the mechanism behind the breakdown of the flat bands as the portion of the moiré cell is reduced at the edges, as well as its relationship with electronic localization, is not clear. To

_____
[*]eandrade@estudiantes.fisica.unam.mx
[†]naumis@fisica.unam.mx

address these questions, in this work we analyze the electronic properties of TBG nanoribbons with different unit cells, ranging from an incomplete to a complete moiré supercell. We consider two nanoribbon geometries: *zigzag* and *armchair* [50,51]. For each configuration, we monitor the electronic localization and the group velocity of the bands near the Fermi energy, and we distinguish between the contributions originating from the moiré scales of those of the graphene lattice. We find that the electronic structure is strongly sensitive to the edge configuration, which may lead to the coexistence or suppression of edge and bulk moiré electronic localization. Our work demonstrates the significant dependence of the electronic structure of twisted bilayer graphene nanoribbons on the edge termination and may offer an explanation for the breakdown of the moiré flat bands found in Ref. [45].

The layout of this paper is as follows. In Sec. II we present the model used, composed of a minimum tight-binding Hamiltonian [52] plus a rescaling approximation. In Sec. III we present our main numerical results concerning *armchair*-terminated TBG nanoribbons, where we analyze the change on the electronic properties as a function of the completeness of the moiré supercell within the ribbon. In Sec. III C we discus the change in energy of the bands as we increase the size of the moiré and explain them qualitatively through a toy model. We also include a brief analysis regarding *zigzag*-terminated TBG nanoribbons in Sec. IV. Finally, in Sec. V we give our conclusions.

II. MODEL

We consider a TBG lattice as shown in Fig. 1(a). The structure is defined by rotating layers 1 and 2 of the *AA*-stacked bilayer around the common center by $\pm\theta/2$, respectively. The lattice vectors of graphene are $a_1 = \sqrt{3}a(0, 1)$ and $a_2 = \sqrt{3}a(\frac{\sqrt{3}}{2}, \frac{1}{2})$, where $a \approx 1.42$ Å is the distance between carbon atoms. Upon rotation, the lattice vectors on each layer are modified as $a_{1,2}^{u/d} = R(\pm\theta/2)a_{1,2}$. We consider a commensurate lattice [26,32] such that the mismatch between layer produces a moiré pattern with lattice vectors given by

$$T_{1/2} = \frac{1}{2\sin(\theta/2)}R(-30°)a_{1/2}. \quad (1)$$

We employ a minimum tight-binding Hamiltonian [52], which consists of an intralayer part $H_{||}$ and an interlayer part $H_\perp$, given by

$$
\begin{aligned}
H &= H_{||} + H_\perp \\
&= -\sum_{i\neq j,m} \gamma_{ij}^{m,m}(c_{m,i}^\dagger c_{m,j} + \text{H.c.}) \\
&\quad - \sum_{i,j,m} \gamma_{ij}^{m,m+1}(c_{m,i}^\dagger c_{m+1,j} + \text{H.c.}),
\end{aligned}
\quad (2)
$$

where $c_{m,i}^\dagger$ and $c_{m,i}$ are creation and annihilation operators, respectively, acting on site i and layer m, and $\gamma_{ij}^{m,m}$ and $\gamma_{ij}^{m,m+1}$ are the intralayer and interlayer hopping integrals, respectively. For the intralayer hoppings only first neighbors are considered, which have a constant value $\gamma_{ij}^{m,m} = t_{||} = 3.09$ eV.
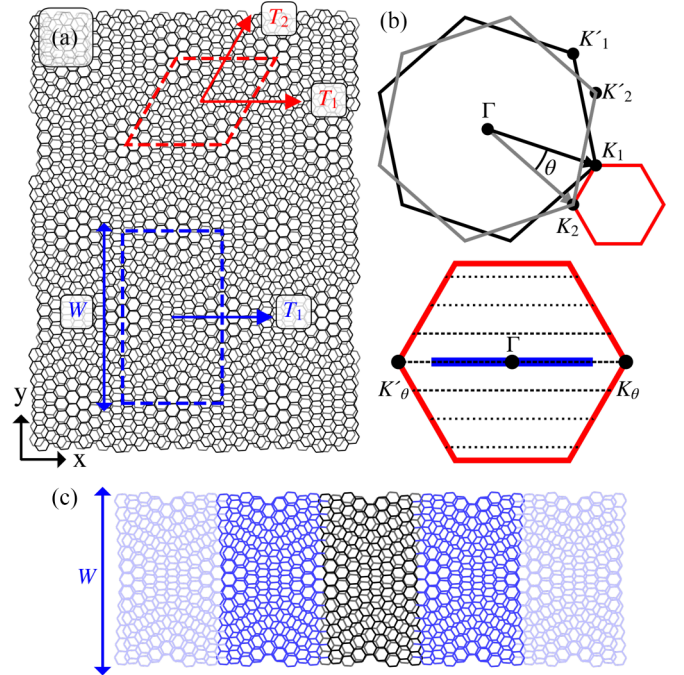

FIG. 1. (a) Lattice structure of TBG with $\theta = 7.34°$, red dashed line is the corresponding unit cell. The blue square cell is used to construct a nanoribbon of width W. (b) Mini-Brillouin zone (red) resulting from the twist between layers. For the nanoribbon the Brillouin gets folded into the blue line as the momentum along the y direction is quantized. (c) Formation of the nanoribbon with the unit cell shown in (a), here five unit cells are shown.

The interlayer hopping is considered to decay exponentially as

$$\gamma_{ij}^{m,m+1} = t_\perp \frac{d_0^2}{r^2 + d_0^2} \exp\left(-\frac{\sqrt{r^2 + d_0^2} - d_0}{\lambda_\perp}\right), \quad (3)$$

where $t_\perp = 0.39$ eV is the hopping amplitude, $d_0 = 3.35$ Å is the distance between layers, and $\lambda_\perp = 0.27$ Å is a modulation of the interlayer hopping.

To reduce the number of atoms and the computational cost in the numerical calculations, we employ a rescaling approximation [53–55], where the bands in TBG depend only on a single dimensionless parameter α given by [35]

$$\alpha = \frac{\sqrt{3}at_\perp}{2\hbar v_f \sin(\theta/2)} \propto \frac{t_\perp}{t_{||}\sin(\theta/2)}, \quad (4)$$

where $t_\perp$ refers to an average of the interlayer hopping and v_f is the Fermi velocity. The importance of this relation is that the dependence on the ratio of the hopping integrals and angle allows us to explore the low-energy physics of a TBG system with a given α using a larger angle and thus reducing the number of atoms in the unit cell. To do this we use a rescaled intralayer hopping integral,

$$t_{||} \to \frac{t_{||}}{\Lambda}, \quad (5a)$$

where

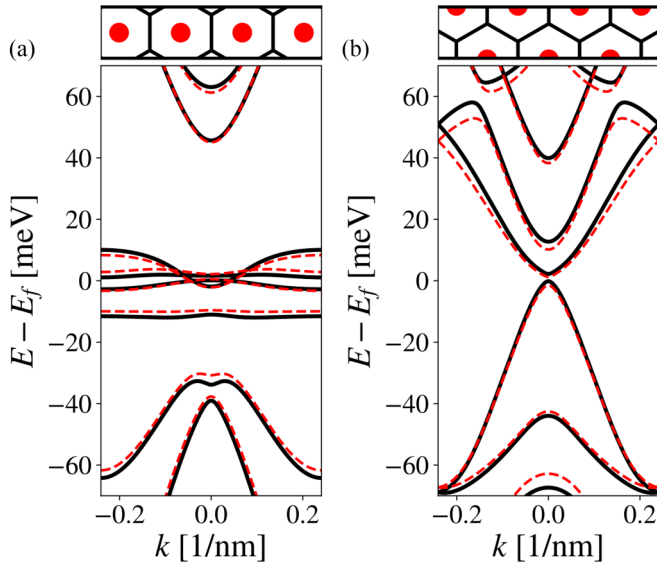$$\Lambda = \frac{\sin(\theta'/2)}{\sin(\theta/2)}. \quad (5b)$$

FIG. 2. Low-energy band structure for a TBG nanoribbon of the width of one moiré cell with twist angle $\theta = 1.08°$ (black solid line) and with $\theta' = 2.28°$ using the rescaling to simulate θ (red dashed line). Above each band structure a schematic of the geometry of each ribbon is shown, where the red circles indicate the AA stacking regions. For (a) the moiré is complete, with the AA regions located at the center of the ribbon. As the moiré cell is complete, states get localized here and flat bands appear around the Fermi energy. In (b) the moirés are split in halves with the AA regions at the edges, and the spectrum around the Fermi energy is dispersive.

In the above equation, θ' is the angle used to simulate the spectrum of a system with angle θ. Furthermore, to preserve the length of the moiré cell, a rescaling of the distances must be done as well,

$$a \rightarrow \Lambda a. \tag{6}$$

This rescaling approximation allow us to simulate the magic angle $\theta = 1.08°$, which has a unit cell of about 11×10^3 atomic sites. In particular, with an angle $\theta' = 2.28°$, which has 5048 atoms, the low-energy band structure is nearly identical to that of the magic angle if we use a scaling factor of $\Lambda = 2.11$ in Eq. (5), thus making computational calculations more attainable.

III. ARMCHAIR-TERMINATED TBG NANORIBBONS

A. Electronic structure

By using the methodology described in the previous section, we first consider the case of *armchair*-terminated TBG nanoribbons. This configuration is the same as that in Fig. 1(c), where the periodicity is along the horizontal direction. In Fig. 2 we show the corresponding spectrum with a single moiré ≈ 11.3 nm considering different moiré terminations. In Fig. 2(a) the AA regions at the moiré center coincide with the ribbon center and the moiré cell is mostly complete; thus the usual localization at the AA regions occurs and flat bands can be seen, in agreement with previous results in TBG flakes [38]. Since the graphene monolayers are

armchair-terminated, the low-energy sates are a mixture of the valley degree of freedom and thus four flat bands appear instead of the usual two. Meanwhile, in Fig. 2(b) the moiré cells are split in halves with the AA regions at the edges. These half-moiré cells are not sufficient to localize the wave function at low energies, and the resulting spectrum is dispersive. In Fig. 3 we further study this transition in ribbons of width $W = 22.6$ nm, around the length of two moirés, ensuring that there is always at least one complete moiré within the ribbon. We characterize different moiré terminations with a sliding parameter δ [46–49], such that it translates the ribbon cell within the TBG lattice, starting from $\delta = 0$, cf. Fig. 3(g), where the moiré is centered with the ribbon, to $\delta = 0.25W$, cf. Fig. 3(l), where the center of the ribbon is between two moirés. In Figs. 3(a)–3(f) we show the energy spectrum around the Fermi energy (E_f) for six different configurations. For each band structure, we show in blue the four lowest energy bands and the next four in red. Note that the sliding structure is periodic in δ such that $\delta = 0.3W$ corresponds to Fig. 3(e) with the unit cell upside down. In Figs. 3(g)–3(l) and Figs. 3(m)–3(r) we show the corresponding total charge density of the bands for each system.

In Fig. 3(a) for $\delta = 0$, there are four narrow bands near E_f which correspond to states mainly localized at the AA regions within the whole moiré cells. There is also localization at the incomplete moirés, but it occurs at higher energies, as shown in Fig. 3(m). Interestingly, by following the sequence of panels in Fig. 3, as we increase δ, the half-moiré cell at the bottom starts to disappear while the upper one grows. Intuitively, the increase in the upper portion of the moiré allows the localization of the wave function in a greater area, lowering its energy towards E_f and also reducing its group velocity. This effect is clearly seen in Figs. 3(a)–3(d), where four red dispersive bands are flattened and pushed towards the center of the energy spectrum, thus increasing their localization in the AA centers, as shown in Figs. 3(g)–3(r).

However, although there is an increase in the size of the incomplete moiré, the red band closer to E_f in Fig. 3(d) is further away in Fig. 3(e), which is also reflected in the absence of hybridization between states of the two moirés in Figs. 3(k) and 3(q). This indicates that the decreasing of the moiré bands energy towards E_f is nonmonotonous. We further explore this behavior in Fig. 4, where we plot the spectrum at the boundary of the Brillouin zone as a function of δ. We observe an oscillatory behavior of the energy bands, which we found to be influenced by the sliding parameter in two distinct ways. Firstly, there is a general tendency of the remote bands to transition from being dispersive to becoming narrow and merge with the flat bands. This occurs near $\delta = 0.25W$. By continuing to increase the sliding parameter, it is equivalent to moving backward in the plot. This large-scale wavelength oscillation has been described as a topological sliding effect in Refs. [46–49]. Secondly, the bands display a short-wavelength oscillation not described before, which we attribute to an interference effect at the atomic scale (cf. Sec. III C).

To analyze these oscillatory effects, in Fig. 4(a) we show the bands for two different ribbon widths (black and blue lines). One thing to notice is that the moiré edge states behave equally for both widths, suggesting that they mainly depend
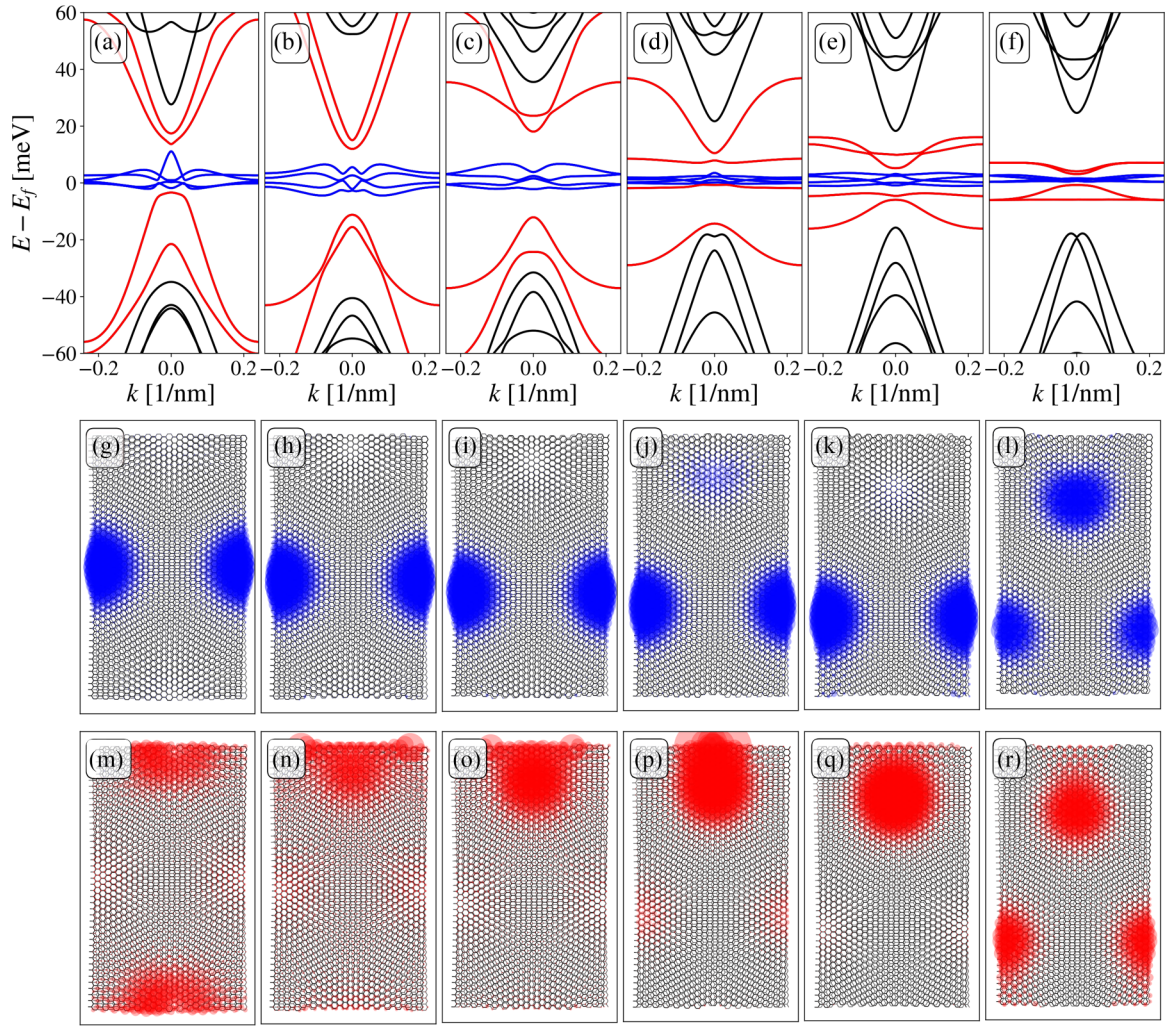
FIG. 3. Low-energy band structure for *armchair*-terminated TBG nanoribbons simulating a twist angle $\theta = 1.08°$ with constant width $W = 22.6$ nm. We consider different moiré terminations by translating the unit cell of the ribbon by (a) $\delta = 0$, (b) $\delta = 0.05W$, (c) $\delta = 0.1W$, (d) $\delta = 0.15W$, (e) $\delta = 0.2W$, and (f) $\delta = 0.25W$. The blue bands are the four lowest energy bands, and these states are localized at the complete moiré. The next four energy bands are shown in red. These correspond to the incomplete moiré, and as we change the termination, increasing the size of the incomplete moiré, the bands get flatter and go towards E_f. In (g)–(l) we show the total charge density of the blue bands respectively to (a)–(f) within the unit cell, while in (m)–(r) for the red bands.

on the completeness of the moiré supercell near the edges. We show a comparison for more widths in Appendix. On the other hand, Fig. 4(b) displays the same bands without the scaling approximation. Thus a comparison between both figures indicates that the long-wavelength oscillations remain unchanged, but the short-wavelength oscillations are different. This suggests that the transition of the bands from being dispersive to becoming narrow is a moiré scale effect and is well captured within the rescaling approximation. Furthermore, we notice that without the rescaling of the atomic distances, the short-wavelength oscillation in Fig. 4(b) is invariant and has a value of $\lambda = \sqrt{3}a/2$. This associates the oscillatory effect to the edges of the microscopic graphene lattice and cannot be effectively mapped with the rescaling approximation. Thus in Fig. 4(a), due to the rescaling the oscillation has a larger wavelength given by $\lambda' = \Lambda\lambda$ in comparison with Fig. 4(b) without rescaling. We further describe this effect in Sec. III C.

B. Charge localization

The effect of an incomplete moiré cell at the edge is depicted in Fig. 5(a), where we show the density of states (DOS) near E_f for the six borders considered in Fig. 3. As δ increases more states move towards E_f due to the completion of the second moiré. In Fig. 5(b) the local density of states (LDOS) for the blue bands in Figs. 3(a)–3(f) is plotted against their y component, with an explicit representation of δ. The black highlighted columns show the location around the *AA* centers of the moiré. As the partial moiré becomes complete, cf. red LDOS in Fig. 5(b), there is a sudden localization of the electrons in the *AA* sites, in agreement with the experiment in Ref. [45].

The previous numerical results suggest that electronic localization plays a paramount role around E_f. To further elucidate its role, we perform a localization analysis using the inverse participation ratio (IPR), which is widely used as a measure of wave-function localization [56–59]. It is
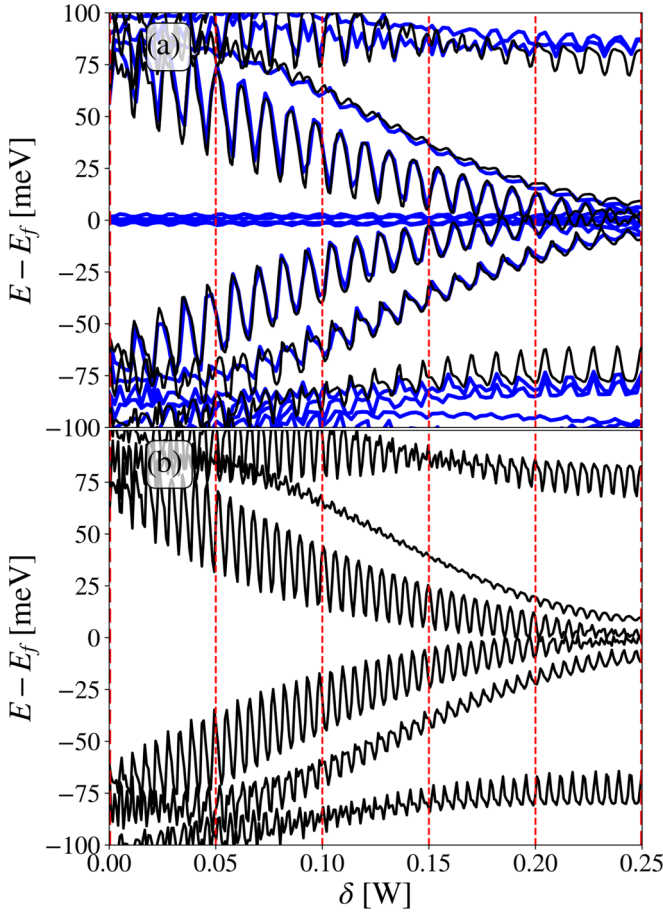
FIG. 4. Spectrum at the edge of the Brillouin zone as a function of δ. (a) The rescaling is used, and we show in black the spectrum for a ribbon of the width of one moiré and in blue for a width of two moirés. It can be seen how the four bands go towards E_f as we increase δ. Furthermore, these bands lower their energy independently of the width of the ribbons, as these bands only depend on the moiré that is being formed at the border. The complete moirés in the bulk will just result in more flat bands around E_f. In (b) for the width of one moiré without rescaling, the wavelength of the oscillation increases as these come from the microscopic borders, which is not equal within the rescaling, but the overall behavior is retained. The dashed red vertical lines indicate the values of δ used in Fig. 3.

FIG. 5. (a) Density of states near E_f for the ribbons shown in Fig. 3, denoted in different colors for $\delta = 0$ (purple), $\delta = 0.05W$ (blue), $\delta = 0.1W$ (green), $\delta = 0.15W$ (yellow), $\delta = 0.2W$ (orange), and $\delta = 0.25W$ (red). The horizontal black lines indicate the offset between the densities. (b) Local density of states (LDOS) of the four nearest bands to E_f [blue bands in Figs. 3(a)–3(f)], plotted against the y component of each site. The ribbons are aligned such that the moiré centers (AA regions) are located at $y = 0$.

defined as

$$\text{IPR}(E) = \sum_i |\psi_{i,k}(E)|^4, \qquad (7)$$

where the sum runs over the atomic sites. For extended states, the $\text{IPR}(E)$ scales as $1/N$, where N is the number of atoms, while for localized states it scales as $\text{IPR}(E) \propto 1/N^0$. A clearer description is obtained by using the normalized IPR, which is defined as [58]

$$\alpha(E) = \frac{\log(\text{IPR}(E))}{\log(N)}, \qquad (8)$$

and thus its range is between -1 and 0. In Fig. 6 we display $\alpha(E)$ for the bands near E_f, using the same color code (blue and red) as in Figs. 3(a)–3(f). Panels (a) and (b) show $\alpha(E)$ for $\delta = 0$ (a whole moiré at the center and moiré halves at
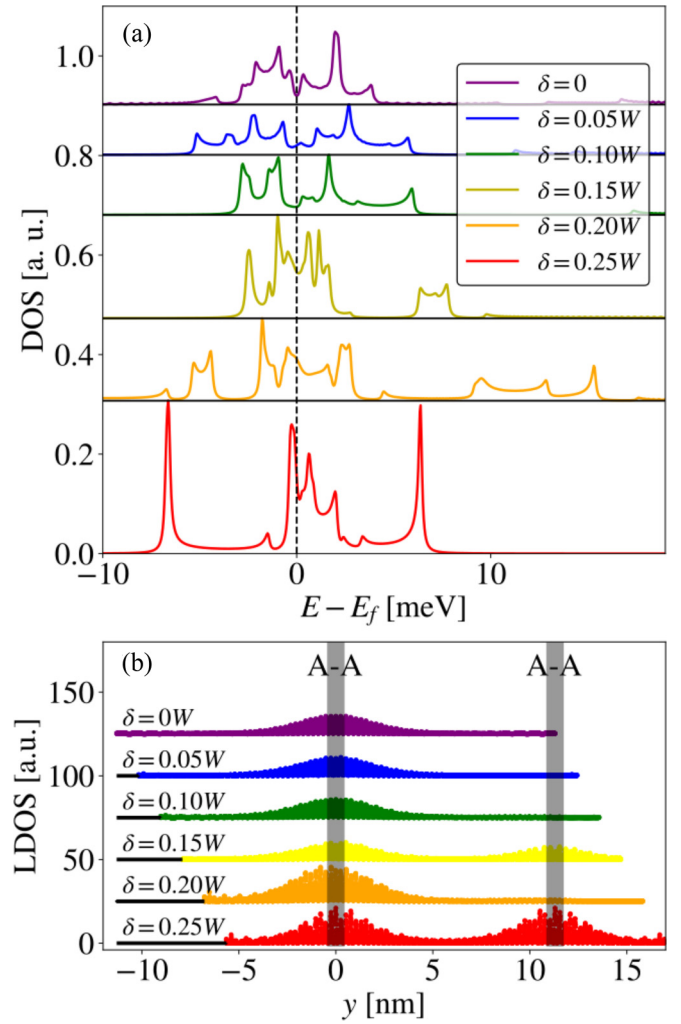
the edges) and $\delta = 0.25W$ (two complete moirés), respectively. As expected, the highest $\alpha(E)$ is located around E_f, corresponding to the flat bands (indicated in blue). It is even greater for $\delta = 0$, as states are localized around just one moiré. The $\alpha(E)$ corresponding to the bands that merge with the flat bands (red bands) change their localization behavior, becoming technically localized as flat bands for $\delta = 0.25W$. All these results suggest that states do have peculiar localization properties around E_f. This is further corroborated in Figs. 6(c) and 6(d), where we display the logarithm of the electron density projected along the nanoribbon cross section. The density tracks the centers of the moiré unitary cells as expected.

Moreover, a recent analysis of TBG continuous models suggests that flat-band states are akin to coherent-Landau states [60–62]. Also, flat-band states in strained graphene nanoribbons have been proved to be pseudo-Landau-level
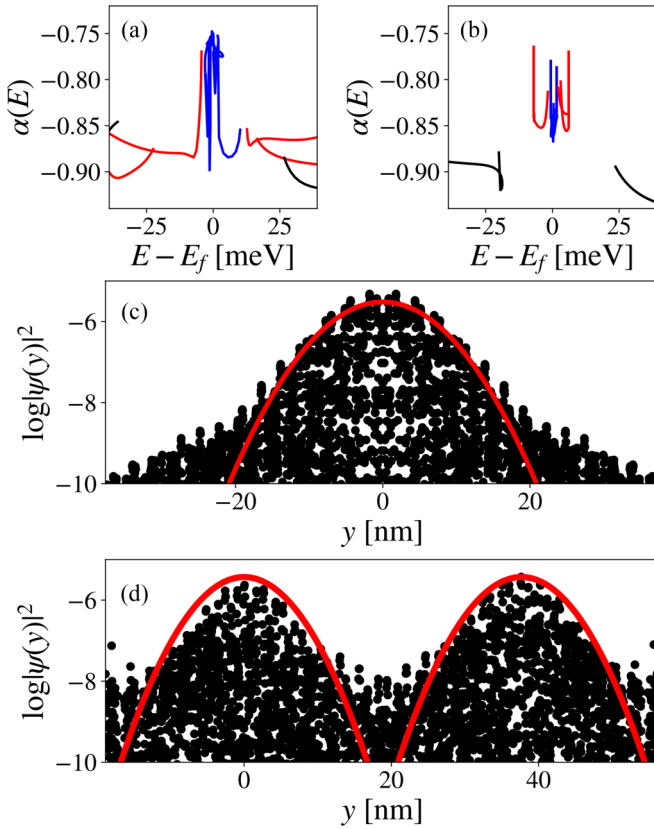
FIG. 6. Normalized inverse participation ratio $\alpha(E)$ for (a) $\delta = 0$ and (b) $\delta = 0.25W$. As expected, the peaks occur around E_f where we have the highly localized states at the AA regions. We show in black dots the logarithm of the numerical probability densities for states near E_f against their y coordinate for (c) $\delta = 0$ and (d) $\delta = 0.25W$. The red line corresponds to a Gaussian probability density in which the standard deviation is chosen to match the IPR of the corresponding state. We can see a good agreement around the localization centers.

states akin to soliton states due to topological boundaries in the Jackiw-Rebbi model [62]. In both cases a nearly Gaussian envelope of the flat-band states was found. This has also been confirmed in calculations that allow factorization of a lowest-Landau-level part in the flat-band wave function [63–66].

Here a nearly Gaussian type of localization can be seen in Figs. 6(c) and 6(d), as the maximal $\log|\psi(r)|^2$ for a given y seems to be limited by downwards parabolas centered at AA sites. Thus we propose a nearly Gaussian wave function with a standard deviation σ such that their IPRs match, i.e., to equate the IPRs of the numerical results we use a Gaussian wave function with σ given by

$$\sigma = \sqrt{\frac{1}{2\pi\,\text{IPR(E)}}}. \tag{9}$$

For each case we pick a state near E_f and plot $\log|\psi(r)|^2$ against its corresponding Gaussian fit, indicated by the red curves in Figs. 6(c) and 6(d) for $\delta = 0$ and $\delta = 0.25W$, respectively. The excellent matching between the red curves and the numerical results near the AA regions indicates a Gaussian behavior in such parts. However, there are clearly fat tails

in Fig. 6(c) when compared with a Gaussian, indicating the particular shape and properties of flat-band functions. These fat tails are a result of the hybridization of the flat bands with the remote bands [67]; they are responsible for the overlap between different AA regions and highlight the interesting nature of flat-band states. Also, the strong tendency for Gaussian localization in AA regions shown here explains why the nanoribbon width does not affect the spectrum very much but instead breaks the AA regions by edges, in agreement with the experiment in Ref. [45]. The strong localization can also be used to estimate the effects of edges using a toy model based on confinement effects, as will be explained in the following section.

C. Toy model: Moiré potential well

As shown in Fig. 4, the lowering of the band energy towards E_f as δ increases is composed of two effects. The first one is the global tendency associated to the confinement. This effect can be explained within the moiré-quantum-well picture, as confined states mainly localized in a quantum well have an energy dependence of $E(L) \propto 1/L^2$, where L is the length of the well. Thus when we increase the parameter δ, the size of the well is increased, and this lowers the energy due to less quantum confinement. We then propose that the energy of the bands localized at the partial moiré have the following δ dependence:

$$E_{AA}(\delta) = E_0 + \frac{AW^2}{(\delta - \delta_0)^2}, \tag{10}$$

where A and E_0 are coefficients to be determined, and $\delta_0 = -0.25W$ is the value where the partial moiré cell vanishes completely. With the numerical data we can use the conditions at $E_{AA}(\delta = 0) = 0$ and $E_{AA}(\delta = 0.25W) = 88$ meV to obtain the coefficients in Eq. (10), which give $A = 7.33$ meV and $E_0 = -29.33$ meV. In Fig. 7(a) we plot the curve given by Eq. (10) using these parameters alongside the numerical results. Clearly, Eq. (10) correctly describes the energy lowering without the oscillating component. As we stated in the previous section, the oscillation wavelength is invariant prior to the rescaling, and this indicates that its origin comes from the graphene lattice. One thing to notice is that due to the rotation angle, the graphene lattice is not aligned with the ribbon's periodicity, and thus there is a discontinuity in the *armchair* edge at which a small *zigzag* border appears. We found that the values of δ at which the oscillation has its local maximums occur when this *zigzag* border lies in the AB regions, while the local minimums occur when it is in the AA regions. In Figs. 7(b) and 7(c) we display the bands and corresponding edges for two values of δ indicated by a square and a circle, respectively, in Fig. 7(a). Both ribbons have moiré cells of roughly the same size.

Therefore we recognize that the position of the *zigzag* border moves periodically as a function of δ, and its periodicity corresponds to λ, the wavelength of the small oscillation in the spectrum. Thus we propose that the *zigzag* edges are responsible for the oscillating perturbation to the spectrum, and we model them as

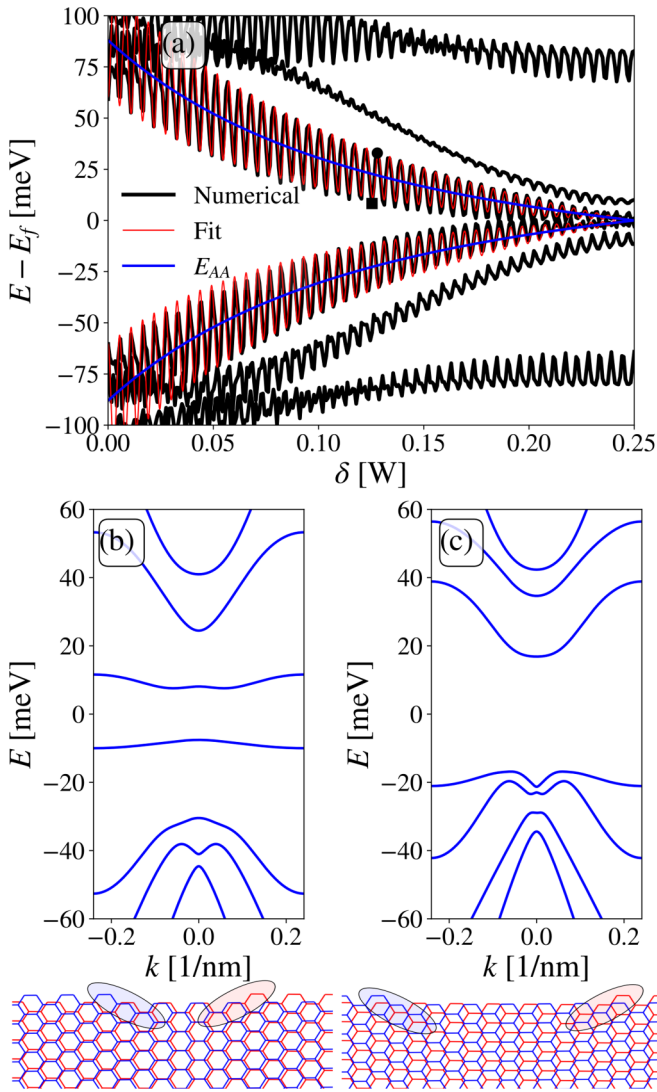$$\Delta E(\delta) = B(e^{-(\delta+\delta_0)/\gamma} - 1)\cos\left(\frac{2\pi\delta}{\lambda}\right). \tag{11}$$

FIG. 7. (a) Energy near E_f of the bands at the Brillouin zone borders for $\theta = 1.08°$ and $W = 11.3$ nm (one moiré cell). The black lines show the numerical results, while the red lines show a fit obtained by considering a change in energy akin to a quantum well as a function of the well's width (blue line), plus an oscillating perturbation originated by the *zigzag* borders. The square and circle markers respectively show the local minimum and maximum for similar values of δ. The low-energy spectrum and the edges of the ribbon are shown for both cases indicated by the markers. In (b) the bands are nearer to E_f and the *zigzag* edges are at *AA* stacking sites, while in (c) the bands are further away from E_f and the *zigzag* edges are at *AB* sites.

Here, B is the amplitude of the perturbation, and γ modulates an exponential decay that we included to control the strength of the perturbation. As the moiré becomes mostly complete, the spectrum is predominantly governed by the moiré well. The energy of these states, mainly localized at the partial moiré, as a function of δ is then

$$E(\delta) = E_{AA}(\delta) + \Delta E(\delta). \tag{12}$$

We found that $B = -32$ meV and $\gamma = 0.4W$ fit the numerical results as shown in Fig. 7(a). Interestingly, the large-scale
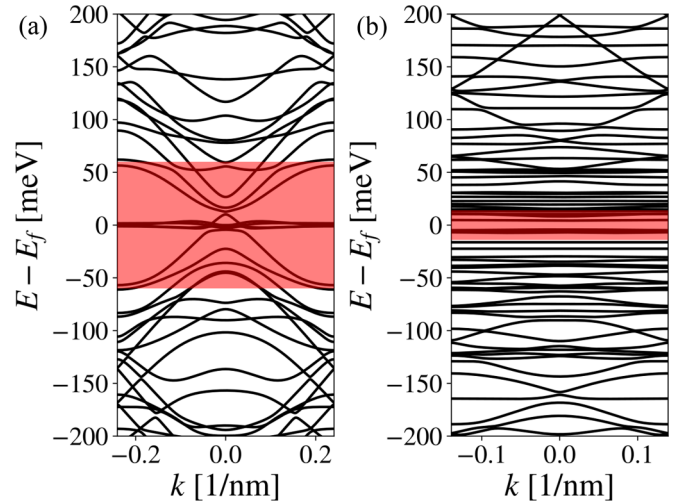

FIG. 8. Energy spectrum for TBG nanoribbons with (a) *armchair* termination and a width $W_{AC} = 22.6$ nm and (b) *zigzag* termination and a width $W_{ZZ} = 13$ nm. Both ribbons are considered with $\delta = 0$ such that each ribbon has a complete moiré at the center and moiré halves at the borders. The red highlighted areas in (a) and (b) show the energy windows at which the spectrum is shown in Fig. 3 and Figs. 9 and 10, respectively.

oscillations that we found are consistent with those reported in Ref. [49]. However, it seems that the impact of the small oscillations was not fully considered. This perturbation of the moiré flat bands has not been reported to our knowledge, and the exact form of the coupling between moiré and edge states still requires further research [42,44]. Furthermore, in a real sample, in regions with *zigzag* edges this coupling will inevitably emerge. Therefore, to complement this work, in the following section we provide a similar analysis to the one shown in Fig. 3 but for *zigzag*-terminated nanoribbons.

IV. ZIGZAG-TERMINATED TBG NANORIBBONS

In this section we investigate the scenario of *zigzag*-terminated TBG nanoribbons. The ribbon's unit cell is illustrated in Fig. 1(c). Unlike the *armchair* case in the previous section, the *zigzag* configuration can be achieved through a translation of a single shaded cell along the y direction. Figure 8 depicts a comparison of the band structure for the nanoribbons of the two considered configurations. The energy bands for the *zigzag* configuration in Fig. 8(b) indicate the presence of low dispersive states even at high energies. In contrast, for the *armchair* configuration in Fig. 8(a), apart from the localized states in the middle of the spectra, there are fewer low dispersive energy states.

In the previous section we found that the states in the small regions with *zigzag* edges, as shown in Figs. 7(b) and 7(c), are responsible for the small oscillations of the moiré bands, as seen in Fig. 7(a). However, the perturbation at the moiré scale is minor and the spectrum is dominated by bulk bands; in this situation, the spectrum for the *armchair* termination clearly shows the flat-band structure of TBG. In contrast, for a *zigzag* nanoribbon, the boundaries generate several edge states
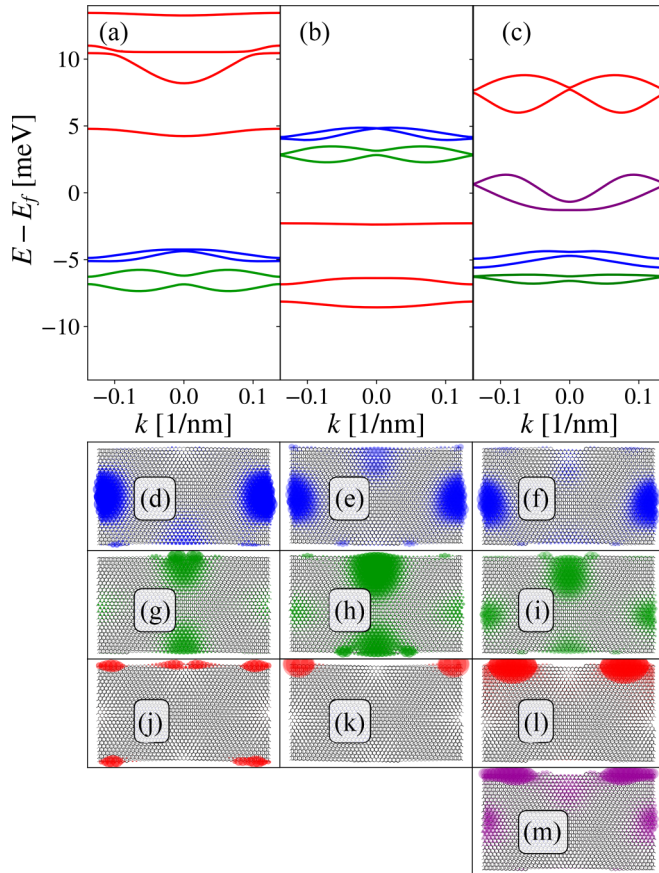
FIG. 9. Low-energy band structure for *zigzag-terminated* TBG nanoribbons simulating a twist angle $\theta = 1.08°$ with constant width $W = 13$ nm but for different moiré terminations obtained by translating the ribbon unit cell by (a) $\delta = 0$, (b) $\delta = 0.05W$, and (c) $\delta = 0.1W$. We color the bands near E_f according to their localization: blue for states localized near the *AA* regions of the mostly complete moiré cells near the center of the ribbon, green for the states localized near the *AA* regions of the incomplete moiré cells near the ribbon edges, red for edge states, and purple for states localized at both *AA* regions and edges. Below each set of bands we plot the corresponding charge density indicated with the same color code.

FIG. 10. Low-energy band structure for *zigzag-terminated* TBG nanoribbons simulating a twist angle $\theta = 1.08°$ with constant width $W = 13$ nm. We consider different moiré terminations by translating the unit cell of the ribbon by (a) $\delta = 0.15W$, (b) $\delta = 0.2W$, and (c) $\delta = 0.25W$. We color the bands near E_f according to their localization, blue for states localized near the *AA* regions, red for edge states, and purple for states localized at both *AA* regions and edges. Below each set of bands we plot the total charge density in the bands of the respective color.

that significantly impact the moiré spectrum, as depicted in Fig. 8(b).

In Figs. 9 and 10 we characterize different moiré terminations by modifying the sliding parameter δ. We ensure that there is always at least one complete moiré within the ribbon. Our focus is on the energy range marked by the red-shaded region in Fig. 8(b). It is worth noting that this energy range is narrower than that of the armchair case due to the denser spectrum near the Fermi energy. Figures 9(a)–9(c) and 10(a)–10(c) depict the band structure for different sliding values. We classify the bands according to their localization: blue for bands mostly localized at the *AA* regions, red for edge states, green for (mixed) states that are a mixture between *AA*-localized and moiré edge states, and purple for those that are a mixture between *AA*-localized and edge states. We notice the difference between moiré edge state and edge state: while the first one is an state mainly localized in an incomplete moiré along the edge (green), the second one is an state mainly
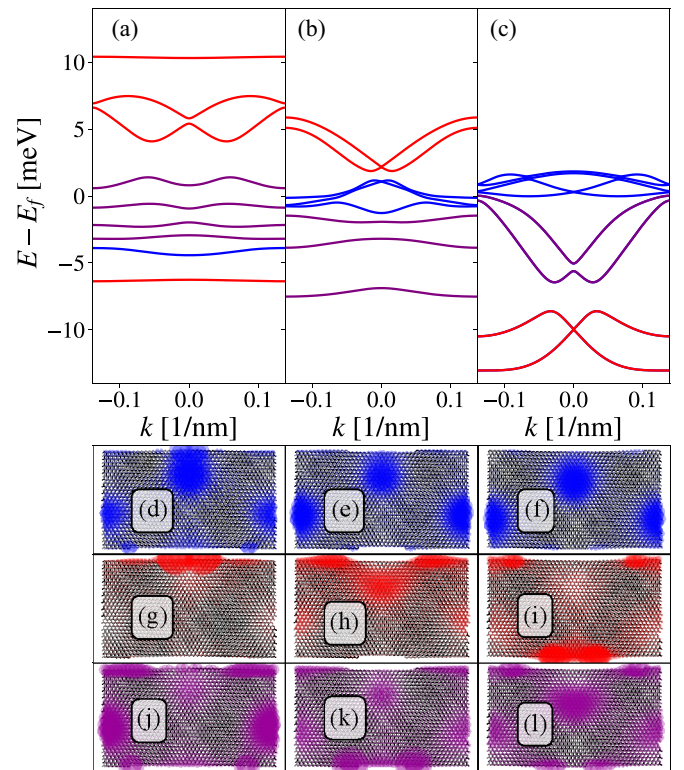
localized on the zigzag sites along the boundary (red). The evolution of the states as the sliding parameter is modified is not as straightforward as in the *armchair* case, as each edge and bulk state has a different energy due to the border geometry. This complexity makes it challenging to differentiate them solely based on their energy and reveals the impact of the edge microscopic boundary in the electronic spectrum.

In Figs. 9(d)–9(m) and Figs. 10(d)–10(l) we show the total charge density for the corresponding band structures. This helps us distinguish the localization of states in the different energy bands. Below each band structure we show the charge density for the bulk, edge, and mixed bands. It is important to note that this classification is not strict; we are using it solely to differentiate the states based on their maximum localization. Under this criterion, as shown in Figs. 9 and 10, is clear that the bulk moiré bands (blue) are mainly localized in the *AA* centers, while the edge states (red) mainly appear at the *AB* regions. These edge states are reminiscent of the monolayer *zigzag* configuration [50,51], and their localization in the *AB* sites is in agreement with experiments in moiré structures of graphite [39,40].

To characterize the different bulk and edge charge contributions, we now perform a localization analysis. Figure 11
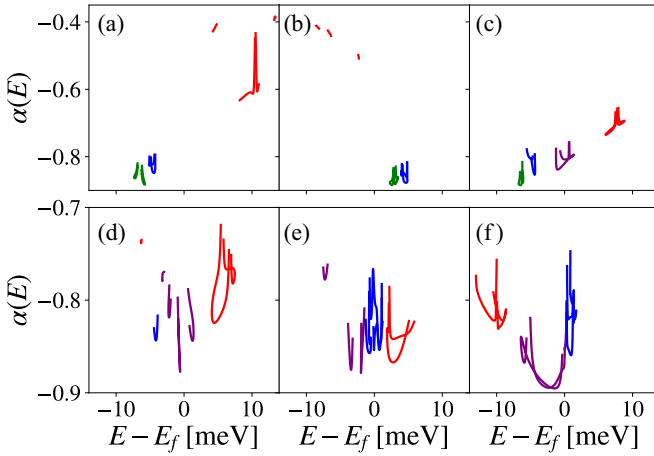
FIG. 11. Normalized inverse participation ratio $\alpha(E)$. Panels (a)–(c) correspond to the bands shown in Fig. 9 and (d)–(f) for the bands in Fig. 10. The color code is the same as in Figs. 9 and 10. As expected, the most localized states usually correspond to edge states (red), as they are distributed between a small number of atoms, especially in (a) and (b). Notice the different scales used between (a)–(c) and (d)–(f). On the contrary, states that are distributed between the *AA* regions and the edges (purple) usually have the lowest value of $\alpha(E)$.

shows the parameter $\alpha(E)$ in Eq. (8) around E_f. In the top panels, the mixed states (green) mostly occupy the incomplete moiré cells with a small contribution from the *AA* centers, cf. Figs. 9(g)–9(i), resulting in a low value of $\alpha(E)$. The values of $\alpha(E)$ for the blue states are just slightly above the green ones, as they are mostly contained within the complete moiré cells. Both blue and green states have a similar value of their $\alpha(E)$ to those of the *armchair* case, as they arise from the moiré pattern. However, the red edge states show a clear difference in magnitude, as they are distributed in a smaller number of atomic sites. In the bottom panels, Figs. 11(d)–11(f), the edge states are not as localized as in the previous case; most of them are partially hybridized with moiré states (notice the difference in the scales). The purple states are highly hybridized moiré and edge states, and thus have the lowest values of $\alpha(E)$ in most cases. The blue states, on the other hand, have their maximum value of $\alpha(E)$ for $\delta = 0.25W$, as this is the point where the two different moiré cells present are mostly complete. Thus the wave function becomes maximally localized within the *AA* regions.

A recent experiment [45] has reported that the low-energy flat band can exist as long as the moiré cell remains complete. Tunneling spectra revealed moiré *AA* spots when the tip was inside the sample. However, an absence of localization due to an incomplete moiré was observed at the boundary. As previously described for an armchair configuration, we have found that the nearly Gaussian localization of the moiré bulk states survives if the moiré is complete, cf. Figs. 6(c) and 6(d), and is suppressed if the moiré is incomplete, cf. Fig. 5(b). This effect is also present in a *zigzag* geometry, where the maximum localization is when the moiré is completed, cf. Fig. 11(f). Interestingly, we found that if the moiré is incomplete, there is an strong hybridization with less localized edge states.

In the experiment described in Ref. [45], the edge orientation predominantly features a zigzag termination. Their results indicated a breakdown of the localized flat bands for an incomplete moiré, and they also reported the presence of edge states in their LDOS maps, aligning with our findings in Fig. 9. These edge states, represented by the red and green states in Fig. 9, manifest as residual LDOS peaks in incomplete moirés and rapidly decay with distance from the edges. The *AA*-localized states only appear in complete moirés, in agreement with the blue states in Fig. 10. Given that the bulk localization is linked to the TBG flat bands, our results demonstrate their sensitivity near the boundaries. Furthermore, for ribbons with widths spanning multiple moiré cells, the flat bands in the bulk remain unperturbed as we modify the borders. We believe that our work comprehensively captures the essential characteristics of both bulk and edge states in TBG nanoribbons, and it offers a detailed explanation for the experimental results in Ref. [45].

V. CONCLUSIONS

In this work we have examined the effects of edges on the electronic properties of twisted bilayer graphene nanoribbons. Using a tight-binding model, we characterized the edge and bulk states in nanoribbons with *zigzag* and *armchair* edge terminations. We found that the flat bands in ribbons with widths spanning multiple moiré cells remain insensitive to edge modifications. However, near the boundaries flat-band localization is sensitive to the edge termination. We observed that the flat band exhibits nearly Gaussian localization, which is suppressed if the moiré is incomplete. Additionally, depending on the edge orientation, bulk states can hybridize with the edge states.

In *armchair*-terminated nanoribbons, the low-energy spectrum is determined by the completeness of the moiré cells at the ribbon's edge, transitioning from dispersive to flat bands as the moiré cell becomes complete. This behavior aligns with a moiré-quantum-well picture. There is also a perturbation in the band's energy due to the appearance of small regions with zigzag termination. Depending on whether these zigzag borders appear on *AA* or *AB* stacking regions, the band energy is either lowered or raised, while the main Gaussian-like localization in the *AA* regions remains. These zigzag regions will inevitably appear due to the mismatch between the ribbon alignment and the armchair direction.

In *zigzag*-terminated nanoribbons, there is a more pronounced impact on the low-energy spectrum due to the edge states, as they can become hybridized with the moiré states. However, some states remain predominantly localized within the *AA* regions. The influence of the edge states is expected to be diminished in real samples as translational symmetry is reduced, resulting in a mixture of armchair and zigzag boundaries. As in the *armchair* case, the behavior should primarily be described by the bands localized within the *AA* regions. Consequently, regardless of the edge termination, we expect *AA* localization when the moiré is complete and delocalization when it is not. Our findings provide an explanation for the breakdown of flat bands and the coexistence of bulk and edge states in recent experiments with twisted bilayer graphene nanoribbons [45].

APPENDIX: SIZE INVARIANCE OF MOIRÉ EDGE STATES

To further elucidate the independence of the moiré edge states to the ribbon's width, in Fig. 12 we show a comparison of the spectrum at the Brillouin zone borders, for different widths, for up to six moiré supercells. It is evident how the four bands converge towards E_f as the moiré supercell at the borders is completed. For widths greater than two moiré cells, there will always be bands at E_f corresponding to the bulk moiré supercells that are complete in the bulk. The spectrum was obtained through a rescaling of a system with $\theta' = 4.41°$, and once again, we observe an impact on the oscillation wavelength. This reinforces the argument that this effect arises from the microscopic graphene lattice.
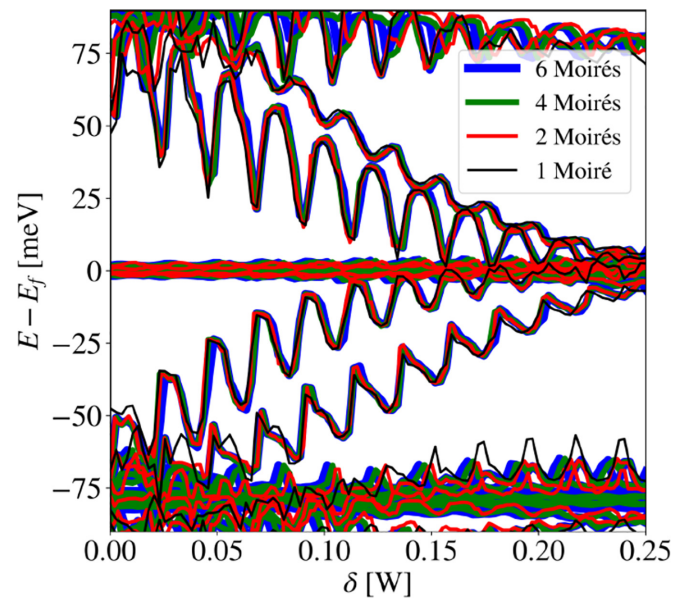

FIG. 12. Spectrum at the edge of the Brillouin zone as a function of δ for multiple nanoribbon widths. Here the spectrum was obtained through a rescaling of a system with $\theta' = 4.41°$ and thus the oscillation wavelength is greater. The figure shows how the moiré edge states behave equally independent from the ribbons width. As the width is increased more supercells can be found within the bulk, resulting in more flat bands at E_f.

[1] Y. Cao, V. Fatemi, S. Fang, K. Watanabe, T. Taniguchi, E. Kaxiras, and P. Jarillo-Herrero, Nature (London) **556**, 43 (2018).

[2] M. Yankowitz, S. Chen, H. Polshyn, Y. Zhang, K. Watanabe, T. Taniguchi, D. Graf, A. F. Young, and C. R. Dean, Science **363**, 1059 (2019).

[3] Y. Cao, V. Fatemi, A. Demir, S. Fang, S. L. Tomarken, J. Y. Luo, J. D. Sanchez-Yamagishi, K. Watanabe, T. Taniguchi, E. Kaxiras *et al.*, Nature (London) **556**, 80 (2018).

[4] K. P. Nuckolls, M. Oh, D. Wong, B. Lian, K. Watanabe, T. Taniguchi, B. A. Bernevig, and A. Yazdani, Nature (London) **588**, 610 (2020).

[5] A. T. Pierce, Y. Xie, J. M. Park, E. Khalaf, S. H. Lee, Y. Cao, D. E. Parker, P. R. Forrester, S. Chen, K. Watanabe *et al.*, Nat. Phys. **17**, 1210 (2021).

[6] A. L. Sharpe, E. J. Fox, A. W. Barnard, J. Finney, K. Watanabe, T. Taniguchi, M. A. Kastner, and D. Goldhaber-Gordon, Science **365**, 605 (2019).

[7] X. Lu, P. Stepanov, W. Yang, M. Xie, M. A. Aamir, I. Das, C. Urgell, K. Watanabe, T. Taniguchi, G. Zhang *et al.*, Nature (London) **574**, 653 (2019).

[8] H. Polshyn, M. Yankowitz, S. Chen, Y. Zhang, K. Watanabe, T. Taniguchi, C. R. Dean, and A. F. Young, Nat. Phys. **15**, 1011 (2019).

[9] M. Serlin, C. L. Tschirhart, H. Polshyn, Y. Zhang, J. Zhu, K. Watanabe, T. Taniguchi, L. Balents, and A. F. Young, Science **367**, 900 (2020).

[10] G. Chen, A. L. Sharpe, E. J. Fox, Y.-H. Zhang, S. Wang, L. Jiang, B. Lyu, H. Li, K. Watanabe, T. Taniguchi *et al.*, Nature (London) **579**, 56 (2020).

[11] Y. Saito, J. Ge, K. Watanabe, T. Taniguchi, and A. F. Young, Nat. Phys. **16**, 926 (2020).

[12] U. Zondiner, A. Rozen, D. Rodan-Legrain, Y. Cao, R. Queiroz, T. Taniguchi, K. Watanabe, Y. Oreg, F. von Oppen, A. Stern *et al.*, Nature (London) **582**, 203 (2020).

[13] D. Wong, K. P. Nuckolls, M. Oh, B. Lian, Y. Xie, S. Jeon, K. Watanabe, T. Taniguchi, B. A. Bernevig, and A. Yazdani, Nature (London) **582**, 198 (2020).

[14] P. Stepanov, I. Das, X. Lu, A. Fahimniya, K. Watanabe, T. Taniguchi, F. H. L. Koppens, J. Lischner, L. Levitov, and D. K. Efetov, Nature (London) **583**, 375 (2020).

[15] Y. Xu, S. Liu, D. A. Rhodes, K. Watanabe, T. Taniguchi, J. Hone, V. Elser, K. F. Mak, and J. Shan, Nature (London) **587**, 214 (2020).

[16] Y. Choi, H. Kim, Y. Peng, A. Thomson, C. Lewandowski, R. Polski, Y. Zhang, H. S. Arora, K. Watanabe, T. Taniguchi *et al.*, Nature (London) **589**, 536 (2021).

[17] A. Rozen, J. M. Park, U. Zondiner, Y. Cao, D. Rodan-Legrain, T. Taniguchi, K. Watanabe, Y. Oreg, A. Stern, E. Berg *et al.*, Nature (London) **592**, 214 (2021).

[18] Y. Cao, D. Rodan-Legrain, J. M. Park, N. F. Q. Yuan, K. Watanabe, T. Taniguchi, R. M. Fernandes, L. Fu, and P. Jarillo-Herrero, Science **372**, 264 (2021).

[19] P. Stepanov, M. Xie, T. Taniguchi, K. Watanabe, X. Lu, A. H. MacDonald, B. A. Bernevig, and D. K. Efetov, Phys. Rev. Lett. **127**, 197701 (2021).

[20] M. Oh, K. P. Nuckolls, D. Wong, R. L. Lee, X. Liu, K. Watanabe, T. Taniguchi, and A. Yazdani, Nature (London) **600**, 240 (2021).

[21] Y. Xie, A. T. Pierce, J. M. Park, D. E. Parker, E. Khalaf, P. Ledwith, Y. Cao, S. H. Lee, S. Chen, P. R. Forrester *et al.*, Nature (London) **600**, 439 (2021).

[22] A. I. Berdyugin, N. Xin, H. Gao, S. Slizovskiy, Z. Dong, S. Bhattacharjee, P. Kumaravadivel, S. Xu, L. A. Ponomarenko, M. Holwill *et al.*, Science **375**, 430 (2022).

[23] S. Turkel, J. Swann, Z. Zhu, M. Christos, K. Watanabe, T. Taniguchi, S. Sachdev, M. S. Scheurer, E. Kaxiras, C. R. Dean *et al.*, Science **376**, 193 (2022).

[24] T. Huang, X. Tu, C. Shen, B. Zheng, J. Wang, H. Wang, K. Khaliji, S. H. Park, Z. Liu, T. Yang *et al.*, Nature (London) **605**, 63 (2022).

[25] P. San-Jose, J. González, and F. Guinea, Phys. Rev. Lett. **108**, 216802 (2012).

[26] J. M. B. Lopes dos Santos, N. M. R. Peres, and A. H. Castro Neto, Phys. Rev. B **86**, 155449 (2012).

[27] G. Trambly de Laissardière, D. Mayou, and L. Magaud, Phys. Rev. B **86**, 125413 (2012).

[28] A. Luican, G. Li, A. Reina, J. Kong, R. R. Nair, K. S. Novoselov, A. K. Geim, and E. Y. Andrei, Phys. Rev. Lett. **106**, 126802 (2011).

[29] L.-J. Yin, J.-B. Qiao, W.-J. Zuo, W.-T. Li, and L. He, Phys. Rev. B **92**, 081406(R) (2015).

[30] Y. Xie, B. Lian, B. Jäck, X. Liu, C.-L. Chiu, K. Watanabe, T. Taniguchi, B. A. Bernevig, and A. Yazdani, Nature (London) **572**, 101 (2019).

[31] Y. Jiang, X. Lai, K. Watanabe, T. Taniguchi, K. Haule, J. Mao, and E. Y. Andrei, Nature (London) **573**, 91 (2019).

[32] J. M. B. Lopes dos Santos, N. M. R. Peres, and A. H. Castro Neto, Phys. Rev. Lett. **99**, 256802 (2007).

[33] S. Shallcross, S. Sharma, and O. A. Pankratov, Phys. Rev. Lett. **101**, 056803 (2008).

[34] S. Shallcross, S. Sharma, E. Kandelaki, and O. A. Pankratov, Phys. Rev. B **81**, 165105 (2010).

[35] R. Bistritzer and A. H. MacDonald, Proc. Natl. Acad. Sci. **108**, 12233 (2011).

[36] G. T. de Laissardière, D. Mayou, and L. Magaud, Nano Lett. **10**, 804 (2010).

[37] E. J. Mele, Phys. Rev. B **81**, 161405(R) (2010).

[38] W. Landgraf, S. Shallcross, K. Türschmann, D. Weckbecker, and O. Pankratov, Phys. Rev. B **87**, 075433 (2013).

[39] E. Suárez Morell, R. Vergara, M. Pacheco, L. Brey, and L. Chico, Phys. Rev. B **89**, 205405 (2014).

[40] E. S. Morell, P. Vargas, P. Häberle, S. A. Hevia, and L. Chico, Phys. Rev. B **91**, 035441 (2015).

[41] H. Shao and G. Zhou, J. Phys.: Condens. Matter **35**, 035301 (2023).

[42] M. Fleischmann, R. Gupta, D. Weckbecker, W. Landgraf, O. Pankratov, V. Meded, and S. Shallcross, Phys. Rev. B **97**, 205128 (2018).

[43] M. Fortin-Deschênes, R. Pu, Y.-F. Zhou, C. Ma, P. Cheung, K. Watanabe, T. Taniguchi, F. Zhang, X. Du, and F. Xia, Nano Lett. **22**, 6186 (2022).

[44] D. Wang, D.-L. Bao, Q. Zheng, C.-T. Wang, S. Wang, P. Fan, S. Mishra, L. Tao, Y. Xiao, L. Huang *et al.*, Nat. Commun. **14**, 1018 (2023).

[45] L.-J. Yin, L.-H. Tong, Y.-Y. Zhou, Y. Zhang, Y. Tian, L. Zhang, L. Zhang, and Z. Qin, Phys. Rev. B **105**, L201405 (2022).

[46] Y. Su and S.-Z. Lin, Phys. Rev. B **101**, 041113(R) (2020).

[47] Y. Zhang, Y. Gao, and D. Xiao, Phys. Rev. B **101**, 041410(R) (2020).

[48] M. Fujimoto, H. Koschke, and M. Koshino, Phys. Rev. B **101**, 041112(R) (2020).

[49] M. Fujimoto and M. Koshino, Phys. Rev. B **103**, 155410 (2021).

[50] M. Fujita, K. Wakabayashi, K. Nakada, and K. Kusakabe, J. Phys. Soc. Jpn. **65**, 1920 (1996).

[51] K. Nakada, M. Fujita, G. Dresselhaus, and M. S. Dresselhaus, Phys. Rev. B **54**, 17954 (1996).

[52] X. Lin and D. Tománek, Phys. Rev. B **98**, 081410(R) (2018).

[53] L. A. Gonzalez-Arraga, J. L. Lado, F. Guinea, and P. San-Jose, Phys. Rev. Lett. **119**, 107201 (2017).

[54] J. Vahedi, R. Peters, A. Missaoui, A. Honecker, and G. T. de Laissardière, SciPost Phys. **11**, 083 (2021).

[55] H. Sainz-Cruz, T. Cea, P. A. Pantaleón, and F. Guinea, Phys. Rev. B **104**, 075144 (2021).

[56] R. Bell and P. Dean, Discuss. Faraday Soc. **50**, 55 (1970).

[57] J. Edwards and D. Thouless, J. Phys. C **5**, 807 (1972).

[58] G. G. Naumis, Phys. Rev. B **76**, 153403 (2007).

[59] P. Shukla, Phys. Rev. B **98**, 054206 (2018).

[60] L. A. Navarro-Labastida and G. G. Naumis, Phys. Rev. B **107**, 155428 (2023).

[61] L. A. Navarro Labastida and G. G. Naumis, Rev. Mex. Fís. **69**, 041602 (2023).

[62] E. Andrade, F. López-Urías, and G. G. Naumis, Phys. Rev. B **107**, 235143 (2023).

[63] G. Tarnopolsky, A. J. Kruchkov, and A. Vishwanath, Phys. Rev. Lett. **122**, 106405 (2019).

[64] F. K. Popov and A. Milekhin, Phys. Rev. B **103**, 155150 (2021).

[65] J. Wang, Y. Zheng, A. J. Millis, and J. Cano, Phys. Rev. Res. **3**, 023155 (2021).

[66] Y. Sheffer and A. Stern, Phys. Rev. B **104**, L121405 (2021).

[67] Z.-D. Song and B. A. Bernevig, Phys. Rev. Lett. **129**, 047601 (2022).